ACS APPLIED POLYMER MATERIALS

pubs.acs.org/acsapm

Article

Humidity-Controlled Preparation of Flexible Porous Carbon Fibers from Block Copolymers

Joel M. Serrano, Glenn A. Spiering, Zhen Xu, Zacary Croft, Dong Guo, Ke Cao, Robert B. Moore, and Guoliang Liu*

Cite This: *ACS Appl. Polym. Mater.* 2022, 4, 4980−4992

Read Online

ACCESS | Metrics & More | Article Recommendations | Supporting Information

ABSTRACT: Growing demands in flexible electronics have stimulated the rapid development of electrodes with multifaceted attributes. Porous carbon fibers (PCFs) provide a potential means to simultaneously achieve flexibility, durability, and energy density. High energy density often necessitates large surface areas and thus pores, but pores generally diminish the mechanical properties. Here, we electrospin poly(methyl methacrylate)-*block*-poly(acrylonitrile) (PMMA-*b*-PAN) and examine the changes in the polymer morphology and resulting PCF porosity and flexibility in response to relative humidity (R.H.). The determining factors of the fiber morphology evolve from block copolymer microphase separation at 40−50% R.H. to vapor-induced phase separation (VIPS) combined with microphase separation at 60−70% R.H. and to vapor-induced precipitation at 80−90% R.H. After pyrolysis, the PCFs show the corresponding porosity, flexibility, and electrochemical properties. Because VIPS enables the polymer fibers to outwardly reorganize PAN and produce continuous graphitic structures, PCFs prepared from polymer fibers electrospun at 70% R.H. develop a mesoporous core and long-range graphitic carbon sheath. Owing to the core−sheath structure, these PCFs exhibit mechanical strength to withstand repeated bending while retaining a 249 ± 20 F g^{-1} capacitance in flexible capacitor assemblies. This work highlights the potential for controlling block copolymer morphologies by processing conditions and PCF properties, providing a platform for designing flexible PCFs for energy and environmental sciences.

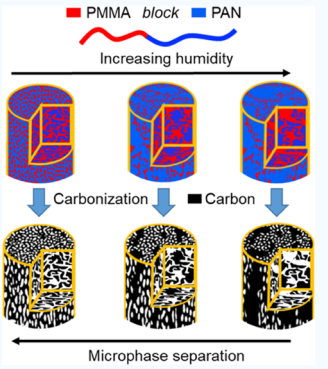

KEYWORDS: *block copolymer, carbon fiber, supercapacitor, polymer morphology, humidity, flexible electronics*

INTRODUCTION

Next-generation electronics demand structural electrodes that have combined high power density, energy density, flexibility, durability, and safety.[1] Structural electrode materials integrating all of these properties are limited.[2,3] Fiber-based electrodes can potentially address structural electronic needs owing to their versatile functionality, flexibility, and strength.[4] Several fiber-based materials have been studied including metal wires,[5] metal composite fibers,[6] conductive polymer fibers,[7] and carbon fibers.[8−10] Traditional metal wires are highly conductive but lack a large surface area to provide high energy density.[11] Metal composite fibers are attractive for their conductivity and multifunctionality (piezoelectrics, nanogenerators, *etc.*); however, their architectures are susceptible to tears and cracks.[12,13] Conductive polymer fibers (*e.g.*, polyaniline (PANI),[7] poly(3,4-ethylenedioxythiophene) (PEDOT),[14] and polypyrrole (PPy)[15]) possess good processability and can be easily integrated with other materials such as cobalt oxide wires,[16] graphene oxides,[17] and polymer binders.[18] However, swelling and shrinking of the conductive polymer fibers cause short electrode life.[19,20] Carbon fibers are known for their superior mechanical strength and have high conductivity similar to metal wires and high redox stability.[21] Therefore, the development of carbon fiber electrodes is desirable for high-performance flexible electrodes.

State-of-the-art carbon fiber electrodes focus on enhancing energy density without compromising the mechanical properties. Enhanced energy density is often achieved with additives/dopants such as nanoparticles,[22] composite layers,[23] and metal oxides.[24] However, pristine carbon fibers have low surface loading of additives/dopants and reduced capacitance due to their small surface areas and porosities.[25,26] Even with exfoliation techniques, surface areas of carbon fibers remain low (typical surface areas of pristine fibers are ∼6 m^2 g^{-1} and exfoliated carbon fibers are ∼92 m^2 g^{-1}).[27] Porous carbon fibers potentially address the issue of low surface area but they often have a reduced mechanical strength.[28] Adding metal wire components ameliorates the strength of porous carbon fibers but detrimentally increases weight and decreases the specific surface area. Therefore, a direct approach to developing porous carbon fibers (PCFs) that retain the mechanical properties (particularly tensile strength and toughness) would allow enhanced energy density and flexibility.

Received: March 28, 2022
Accepted: June 3, 2022
Published: June 16, 2022

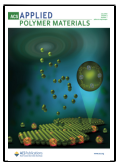

https://doi.org/10.1021/acsapm.2c00534
ACS Appl. Polym. Mater. 2022, 4, 4980−4992

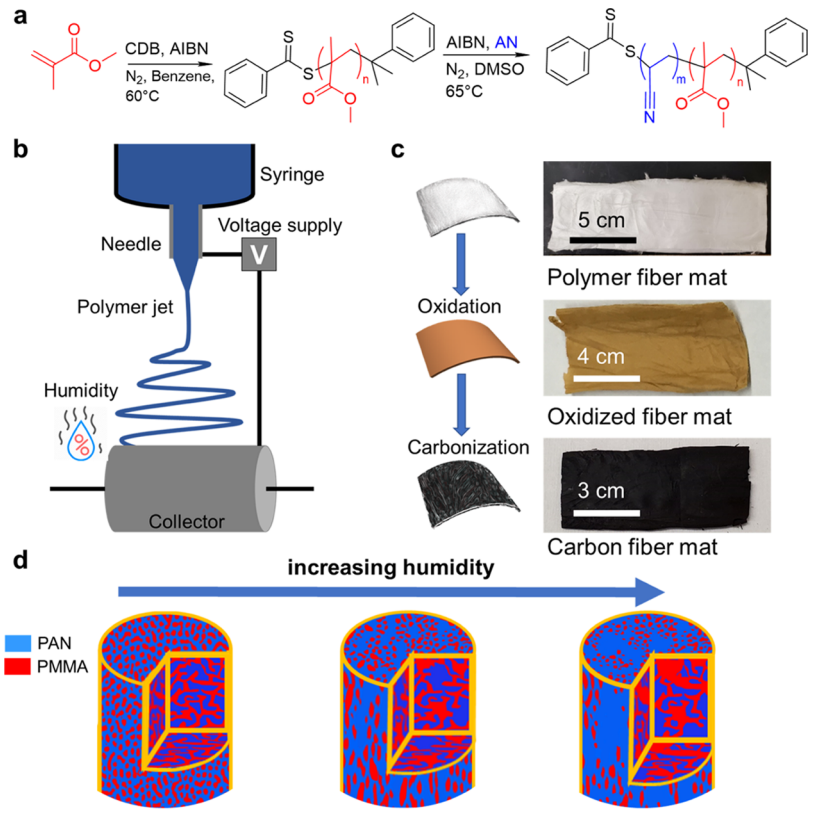

Figure 1. (a) PMMA-*b*-PAN was synthesized *via* controlled radical polymerization using cumyl dithiobenzoate (CDB), azobisisobutyronitrile (AIBN), acrylonitrile (AN), and dimethyl sulfoxide (DMSO). (b) PMMA-*b*-PAN was electrospun into fiber mats under conditions of varying humidities. (c) PMMA-*b*-PAN fiber mats were oxidized at 280 °C and subsequently carbonized at 800 °C. The photographs show representative fiber mats after each step. (d) Due to the presence of nonsolvent water vapor, upon increasing humidity, the determining factors of PMMA-*b*-PAN morphologies evolve from block copolymer microphase separation to VIPS and to vapor-induced precipitation.

High-mechanical-strength carbon fibers are typically made from polyacrylonitrile (PAN) because of the long-range graphitic carbon, but certain pore fabrication methods can disrupt the graphitic structure. For example, PAN blended with sacrificial polymers such as poly(styrene) (PS)[29] and poly(methyl methacrylate) (PMMA)[30] leads to broad pore/graphitic carbon distribution during carbonization, whereas PAN-based copolymers reach even higher porosity and surface area with narrow pore/graphitic carbon distribution in the resulting PCFs.[31,32] The high degree of porosity and narrow pore distributions might disrupt long-range graphitic structures and compromise the mechanical properties.[33−35] Recently, our laboratory has developed PCFs from poly(methyl methacrylate)-*block*-poly(acrylonitrile) (PMMA-*b*-PAN).[32] Owing to the block copolymer microphase separation and the narrowly dispersed mesopores, these PCFs have shown outstanding capabilities for energy storage.[36] However, the mechanical properties remain to be elucidated.[37] Interestingly, in the preparation of separation membranes, vapor-induced phase separation (VIPS)[38,39] has shown the potential to generate pores in polymers while retaining excellent mechanical strength.[40] VIPS can tune the crystalline morphology of polymers and maintain the mechanical properties.[41] However, the effects of VIPS on the PAN-based block copolymer and carbon fibers are unknown.[42,43] We hypothesize that the synergistic integration of block copolymer microphase separation with VIPS may provide uniform mesopores and retain long-range graphitic structures in PCFs to ensure both high energy density and mechanical strength.

Herein, we study the morphologies of electrospun PMMA-*b*-PAN fibers in relative humidity (R.H.) of 40−90% to investigate synergistic microphase separation and VIPS (Figure 1). Water vapor acts as a nonsolvent to induce the VIPS effect and reorganize the polymer morphology in the electrospun fibers. The reorganization develops PMMA and PAN structures that directly influence the PCF physical, mechanical, and electrochemical properties. At lower humidity (40−50%), the polymer fibers mainly undergo block copolymer microphase separation, which develops into uniform mesopores. At mid-range humidity (60−70%), the polymer fibers show the reorganization of PAN toward sheath and PMMA to the core, which results in a carbon sheath and larger internal pores. At high humidity (80−90%), the polymer fibers develop beads and clumps during electrospinning due to nonsolvent vapor-induced precipitation. By systematically studying the effect of humidity on the block copolymer fiber morphology, we highlight the tunability of PCF properties for use as a flexible electrode.

MATERIALS AND METHODS

Chemicals. Methyl methacrylate (MMA, ≥99%), acrylonitrile (AN, ≥99%), azobisisobutyronitrile (AIBN, ≥98%), benzene (≥99%), aluminum oxide (activated, neutral, Brockmann Activity I), *N*,*N*-dimethylformamide (DMF, ≥99.7%), and dimethyl sulfoxide (DMSO, ≥99.9%) were purchased from Sigma-Aldrich. Cumyl dithiobenzoate (CDB) was synthesized *via* a previously reported protocol.[32] Methanol (Pharmco-AAPER) was used for polymer precipitation. Nickel foam (MTI Corporation) was used as electrode

https://doi.org/10.1021/acsapm.2c00534
ACS Appl. Polym. Mater. 2022, 4, 4980−4992

substrates. Inhibitors in MMA and AN were removed by alumina columns; all other chemicals were used as received.

Preparation of PCFs. PMMA-*b*-PAN was synthesized *via* reversible addition−fragmentation chain-transfer (RAFT) polymerization modified from a previous report.[32,36,37,44,45] First, MMA (70.0 mL, 618 mmol), CDB (169 mg, 0.318 mmol), and AIBN (50.8 mg, 0.310 mmol) were dissolved in benzene (120 mL) in a 1 L Schlenk flask. The mixture was subjected to four cycles of freeze−pump−thaw (FPT) followed by back-filling with N_2 to remove the dissolved oxygen. The reaction proceeded at 60 °C for 27 h, resulting in a PMMA macro-chain-transfer agent (macro-CTA). The macro-CTA was precipitated in methanol, filtered, and dried in air for 24 h. The purified macro-CTA (65.0 g, 1.08 mmol) was then mixed with AN (260 mL, 4.33 mol), AIBN (4.40 mg, 270 μmol), and DMSO (700 mL) into a 2 L Schlenk flask to synthesize PMMA-*b*-PAN. The mixture was degassed by four FPT cycles and then heated in an oil bath at 65 °C under a N_2 atmosphere for 24 h. The resulting PMMA-*b*-PAN block copolymers were purified following the same steps as those of PMMA macro-CTA. The number average molecular weights (M_n) and polydispersity index (PDI) were measured with size exclusion chromatography (SEC) (EcoSEC HLC-8320GPC) equipped with a light scattering detector (DynaPro Nanostar photometer).

PMMA-*b*-PAN (M_n = 171 kDa, PDI = 1.11) (Figure S1) was dissolved in DMF at a concentration of 17 wt %. The dissolved PMMA-*b*-PAN was electrospun at an injection rate of 0.020 mL min^{-1} and a voltage bias of 18 kV provided by a high-voltage supply (Model P030HP1, Acopian Technical Company) similar to previous protocols.[32] Electrospun fibers were collected by an aluminum drum with a rotating speed of ∼280 rotations per minute (rpm). The entire apparatus was placed within a transparent epoxy chamber equipped with a humidifier and a hygrometer to tune humidity during electrospinning. Relative humidity (R.H.) to room temperature (∼23 °C) was set to 40, 50, 60, 70, 80, and 90% with a ±3% tolerance to electrospin six sets of polymer fiber mats. All other electrospinning conditions (except the relative humidity) remained the same for all electrospun fiber mats in this study. The oxidized and carbonized fibers were designated as oxidized or PCFs with their corresponding R.H. during the polymer fiber preparation step throughout this paper (Table 1). The as-spun fibers were oxidized and stabilized at 280 °C for 8 h (heating ramp rate, 1 °C min^{-1}) in air and then pyrolyzed at 800 °C (heating ramp rate, 10 °C min^{-1}) for 1 h in an electrical tube furnace (Model STF55433C-1, Lindberg/Blue M) with a constant N_2 flow of 200 standard cubic centimeters per minute (sccm). The resultant PCFs were used without further activation.

Material Characterizations. The fibers were imaged with a scanning electron microscope (LEO Zeiss 1550 SEM, acceleration voltage: 2−4 kV, working distance: ∼3 mm). Because of inadequate electrical conductivity, the as-spun and oxidized fibers were coated with ∼4 nm iridium prior to scanning electron microscopy (SEM) imaging. N_2 and CO_2 physisorptions were conducted at 77 and 273 K, respectively, on a 3Flex Pore Analyzer (Micrometric Instruments Company). Prior to physisorption, PCFs were degassed at 90 °C for 1 h and 300 °C for 10 h to remove any potential adsorbents on the carbon surfaces. Surface areas were calculated based on the Brunauer−Emmett−Teller (BET) theory. Pore size distributions were obtained using nonlocalized density functional theory (NLDFT), similar to previous reports.[32] The mechanical properties were evaluated based on the cross-sectional area of the fiber mats, which were placed under tension. The fibers were tested with dynamic mechanical analysis (DMA) with fiber mats in the tensile mode. Calipers with ±0.01 mm were used to measure the cross-sectional area.

Electrochemical Characterizations. All electrochemical tests were performed on a PARSTAT 4000+ electrochemical workstation (Princeton Applied Research, AMETEK Inc.) with a three-electrode testing configuration. PCFs (∼2−3 mg) were placed between two pieces of nickel foam (∼1 × 3 cm^2) so that only the top portion of the PCFs was in contact with the nickel foam. The electrodes were then pressed at 4 metric tons using a benchtop hydraulic shop press (Stongway, Model 46269). The actual mass loading of PCFs was measured using an analytical balance (Model Mettler Toledo XSE105) with a sensitivity of ±0.01 mg. The mass was checked before and after pressing to account for any material loss during the pressing process.

Table 1. Nomenclature of the Polymer, Oxidized, and Carbonized Fibers Used in This Study[a]

relative humidity during electrospinning (%)	treatment process	designation
40	none—as-spun	40% polymer fibers
50	none—as-spun	50% polymer fibers
60	none—as-spun	60% polymer fibers
70	none—as-spun	70% polymer fibers
80	none—as-spun	80% polymer fibers
90	none—as-spun	90% polymer fibers
40	oxidized at 280 °C	40% oxidized fibers
50	oxidized at 280 °C	50% oxidized fibers
60	oxidized at 280 °C	60% oxidized fibers
70	oxidized at 280 °C	70% oxidized fibers
80	oxidized at 280 °C	80% oxidized fibers
90	oxidized at 280 °C	90% oxidized fibers
40	carbonized at 800 °C	40% PCFs
50	carbonized at 800 °C	50% PCFs
60	carbonized at 800 °C	60% PCFs
70	carbonized at 800 °C	70% PCFs
80	carbonized at 800 °C	80% PCFs
90	carbonized at 800 °C	90% PCFs

[a]Note that the polymer fibers are as-spun and the oxidized and carbonized fibers are processed at 280 °C and 800 °C, respectively.

The PCF electrodes were then tested using cyclic voltammetry (CV) to evaluate the electrochemical performance. A Ag/AgCl electrode (in saturated KCl aqueous solution) and a piece of nickel foam were used as the reference and counter electrodes, respectively. The electrolyte was a 3 M KOH solution for electrochemical tests. CV curves were collected within a potential window from 0 to −0.8 V *vs* Ag/AgCl at various scan rates between 10 and 1000 mV s^{-1}. The PCF gravimetric capacitances from CV were calculated using the following equation[44]

$$C = \frac{1}{2(V_t - V_0)v} \int_{V_0}^{V_t} |I_m(V)| dV \quad (1)$$

where $I_m(V)$ is the current density (A g^{-1}), v is the scan rate (mV s^{-1}), and V_0 and V_t are the lower and upper potential limits of the potential window, respectively. For the flexible supercapacitors, a quasi-solid-state electrode was created with PCF electrodes and a PVA/KOH electrolyte. A solution of poly(vinyl alcohol) (PVA) (M_w ∼ 35 kDa) and deionized water (1:2 wt ratio) was mixed for 2 h in a flask at 80 °C. Once the solution appeared homogeneous, 10 mL of 6 M KOH solution was added and mixed for 15 min. The solution was then poured into a glass Petri dish, which contained two symmetric PCF electrodes. Once the electrodes were fully submerged, the Petri

https://doi.org/10.1021/acsapm.2c00534
ACS Appl. Polym. Mater. 2022, 4, 4980−4992

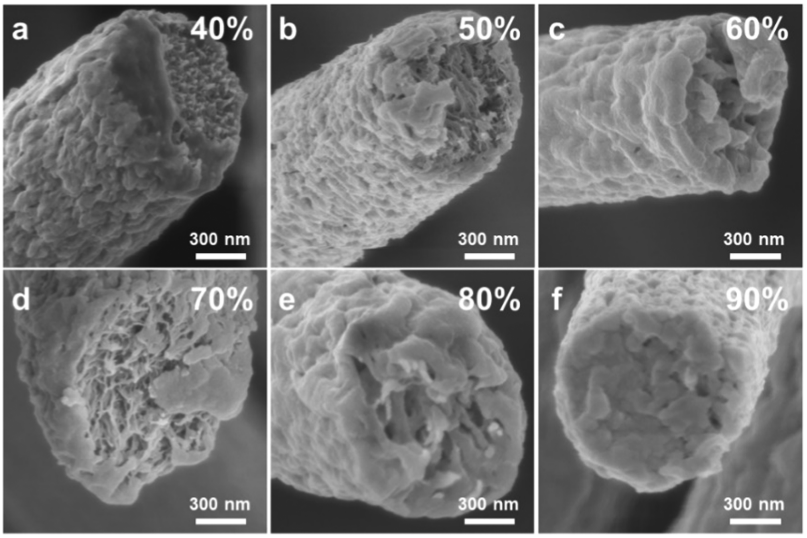

Figure 2. Representative SEM images of PMMA-*b*-PAN fibers immediately after electrospinning under R.H. of (a) 40%, (b) 50%, (c) 60%, (d) 70%, (e) 80%, and (f) 90%.

dish containing PCF electrodes and PVA/KOH was placed in a freezer for 2 h. The subsequent quasi-solid-state gel electrode was then tested with CV with a two-electrode setup from 0 to 1.1 V at scan rates of 10−1000 mV s^{-1}. The gravimetric capacitance was calculated with 1.

Ultra-Small-Angle X-ray Scattering (USAXS)/Small-Angle X-ray Scattering (SAXS) Characterization. Ultra-small-angle X-ray scattering (USAXS)/small-angle X-ray scattering (SAXS) measurements were collected at beamline 9-ID-C at the Advanced Photon Source (APS) at Argonne National Laboratory (Lemont, Illinois).[46] Samples were mounted between two pieces of 3M Scotch tape. The X-ray energy was 21 keV, and the X-ray wavelength was 0.5904 Å. Data were acquired over 90 s for USAXS and 20 s for SAXS. The beam size was 0.8 × 0.8 mm^2 for USAXS and 0.8 × 0.2 mm^2 for SAXS. Data were reduced and corrected for background, thickness, and transmission using the Indra[47] and Nika[48] programs for Igor Pro. The data were output on an absolute scale. The Irena program for Igor Pro was used to merge same-specimen USAXS and SAXS profiles,[47] yielding a continuous scattering vector (q) range from 0.001 to about 16 nm^{-1}. Scattering plots are presented as scattering intensity, $I(q)$, versus scattering vector q, where $q = (4\pi/\lambda)\sin(\theta)$, θ is one-half of the scattering angle, and λ is the X-ray wavelength. Slit-smeared USAXS data were desmeared using Indra, yielding pinhole equivalent data. Merged USAXS/SAXS profiles were fit to the Unified Fit[49] function using Irena.

Unified Fit. The Unified Fit function[49] is used to fit multiple populations of scatterers each with a Guinier knee and a power-law decay. A single level can be expressed as

$$I_i(q) = G_i\, e^{-q^2R_{g,i}^2/3} + e^{-q^2R_{gco,i}^2/3}B_i\left\{\frac{\left(\mathrm{erf}\left(\frac{kqR_{g,i}}{\sqrt{6}}\right)\right)^3}{q}\right\}^{P_i} \quad (2)$$

where q is the scattering vector, $I_i(q)$ is the intensity of the ith level as a function of q, G_i is the Guinier prefactor, B_i is the power-law prefactor, erf is the error function, and $_{Pi}$ is the Porod exponent. $R_{gco,i}$ is a high q cutoff for the power law, typically equal to $R_{g(i-1)}$. The term k is 1 for surface fractals and 1.06 for mass fractals. $R_{g,i}$ is the radius of gyration of the scatterer, which quantifies the size of a scatterer independent of the scatterer's shape.[63] Many levels are summed as

$$I(q) = \sum_{i=1}^{N}\left[G_i\, e^{-q^2R_{g,i}^2/3} + e^{-q^2R_{gco,i}^2/3}B_i\left\{\frac{\left(\mathrm{erf}\left(\frac{qR_{g,i}}{\sqrt{6}}\right)\right)^3}{q}\right\}^{P_i}\right] \quad (3)$$

The Unified Fit can be modified to accommodate for a weak structure factor. The Born−Green closure of the Ornstein−Zernike equation is used to modify the scattering pattern[50]

$$S(q) = \frac{1}{1 + p \times \theta(q, \eta)} \quad (4)$$

where $S(q)$ is the structure factor, p is the packing factor, and $\theta(q, \eta)$ is the spherical amplitude function

$$\theta(q, \eta) = 3\frac{\sin(q\eta) - q\eta\cos(q\eta)}{(q\eta)^3} \quad (5)$$

where η is the radial correlation distance.[51] $S(q)$ is multiplied to $I_i(q)$ to include structure factor contributions to the desired level in the Unified Fit function.

RESULTS AND DISCUSSION

Electrospinning and Fiber Morphology. Block copolymer-derived porous carbon fibers showed a high degree of control over the pore structure, surface area, and electrochemical properties.[32] Physical properties of the porous carbon fibers can also be tuned by the volume fractions of the constituent blocks and the molecular weight of the block copolymers.[32] In our previous reports,[36,43,44] electrospun PMMA-*b*-PAN fibers exhibited kinetically trapped microphase separation of PMMA and PAN. The polymer morphology carried over to the resulting porous carbon fibers, but the effects of solvent/nonsolvent on block copolymer phase separation in fibers have not been fully elucidated. In addition, the morphological structures require further investigation in the electrospun polymer fibers, oxidized fibers, and carbon fibers.

Humidity serves as a nonsolvent vapor that directly influences the morphology and domain size in block copolymer fibers. Here, the PMMA-*b*-PAN fibers were subject to various electrospinning conditions under 40−90% R.H. The electrospun polymer fibers, oxidized fibers, and carbon fibers

https://doi.org/10.1021/acsapm.2c00534
ACS Appl. Polym. Mater. 2022, 4, 4980−4992

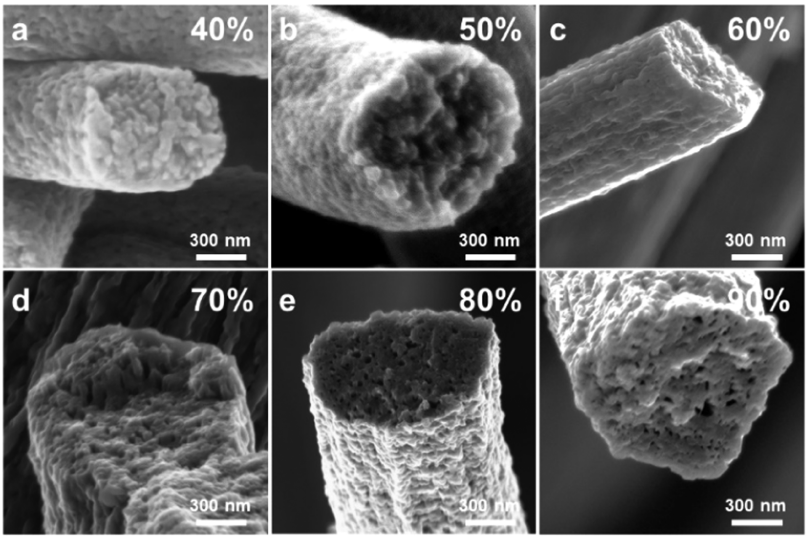

Figure 3. Representative SEM images of PMMA-*b*-PAN fibers after oxidization at 280 °C. The polymer fibers were electrospun under R.H. of (a) 40%, (b) 50%, (c) 60%, (d) 70%, (e) 80%, and (f) 90%.

are designated by the humidity levels during electrospinning and current thermal processing steps (*e.g.*, 40% polymer fibers, 70% oxidized fibers, *etc.*) (Table 1). The 40% polymer fibers showed well-dispersed domains (Figure 2a). The fiber skin appeared slightly smeared after the electrospinning flight. The 40 and 50% polymer fibers shared similar morphologies in the cross section with microphase separation of PMMA and PAN (Figure 2a,b). The 60% polymer fibers exhibited PAN sheath development on the fiber surface (Figure 2c). The 70% polymer fibers also showed a PAN sheath layer, and the microphase separation was still visible in the cross section (Figure 2d). Lastly, the 80 and 90% polymer fibers showed tantamount PAN sheath development. In addition, larger pores appeared inside the polymer fibers, possibly due to an effect of nonsolvent-induced precipitation.[52,53]

The humidity also affected the structure of the fibers with regard to fiber alignment. At a low drum-rotation rate of ∼280 rpm, the fibers lacked significant alignment but were still marginally aligned in the axial direction owing to the drum-shaped fiber collector. The 40−70% polymer fibers retained the individual fiber shape, and these fibers shared a similar fiber alignment (Figure S2). However, the 80−90% polymer fibers showed a different structure with much less axial alignment. The adjacent fibers tended to fuse either intersectionally or parallelly (Figure 2Se,f).

The block copolymer phase separation is of paramount importance for the physical, mechanical, and electrochemical properties of the resulting PCFs. Typically, lower humidity levels barely affected the solvent evaporation and thus the fibers exhibited kinetically trapped PAN and PMMA domains,[54] similar to the electrospun PMMA-*b*-PAN fibers in our previous reports.[32,36] The higher humidity levels, however, induced a nonsolvent effect on the polymer jets and disrupted the block copolymer microphase separation. Thus, the PMMA-*b*-PAN fibers possessed complex phase-separated structures arising from the combined effects of solvent evaporation, nonsolvent VIPS, and block copolymer microphase separation. First, SEM displayed a trend of PAN reorganization toward the sheath and PMMA migration toward the core, possibly driven by the greater hydrophobicity[55,56] and surface energy[56] of PMMA than those of PAN. Surface energies of PMMA and PAN are ∼41 and ∼27 mN m^{-1}, respectively.[56] In addition, PAN domains were subject to electrostatic repulsion within the jet stream during electrospinning, and thus the PAN domains reorganized along the sheath of the fiber.[57] Furthermore, a "polymer precipitation" effect was visible in the 80−90% polymer fibers, where polymer clumps formed because of the high-humidity levels (Figure S3). The clump formation is a known complication in electrospinning that accompanies nonsolvent vapor (*i.e.*, humidity).[31] Lastly, the high humidity also reduces the speed at which the solvent (DMF) evaporates from the fibers, thereby providing the polymer chains with mobility to reorganize. The reorganization in high humidity allows PMMA-*b*-PAN to reach better microphase separation than the kinetically trapped morphologies in lower humidity.[58]

Oxidation provides stability for the polymer fibers prior to carbonization and induces block copolymers to microphase-separate and reorganize.[59] Previous reports have shown that oxidation partially degrades PMMA into pores and cross-links PAN into a network structure.[36] The 40−50% oxidized fibers retained the PMMA and PAN domains derived from the polymer fibers, and both the skin surface and cross section showed relatively uniform pores (Figure 3a,b). However, in 60% oxidized fibers, portions of the PMMA domains coalesced and developed into nonuniform pores with greater dispersity than in 40−50% oxidized fibers (Figure S4c). Portions of the PAN domains developed into ridges along the fiber sheath (Figure 3c). The 70% oxidized fibers showed the coalescence of PMMA escalated, and the nonuniform pores were more prevalent in both the cross section and skin surface (Figures 3d and S4d). The pore nonuniformity was the most apparent in 80−90% oxidized fibers, as depicted by the large voids (Figure 3e,f). A zoomed-out view of the 80−90% oxidized fibers showed that they retained the fused structures from the as-spun fibers (Figure S5).

Carbonization decomposed PMMA and completed the PAN cross-linking, which solidified the final morphology into a porous carbon network *via* pyrolysis. The 40−50% PCFs resembled our previously reported PMMA-*b*-PAN-derived carbon fibers prepared under similar conditions.[35] These carbon fibers consisted of the typical porous structures

https://doi.org/10.1021/acsapm.2c00534
ACS Appl. Polym. Mater. 2022, 4, 4980−4992

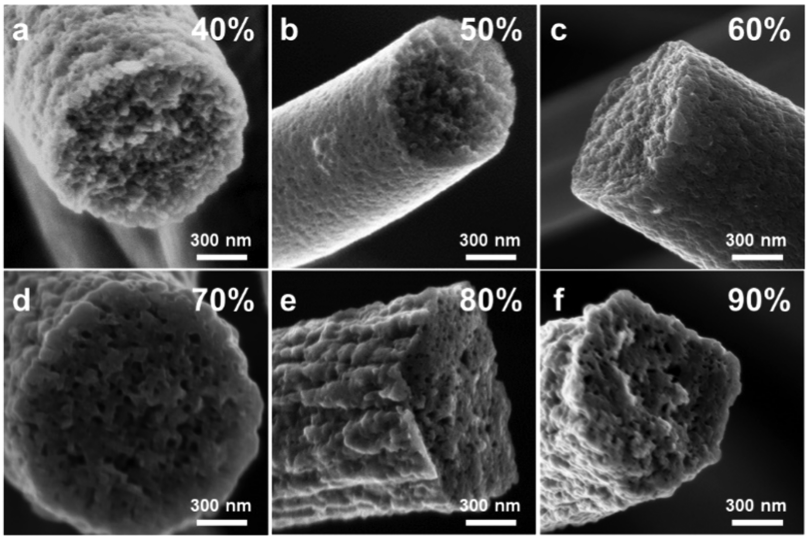

Figure 4. Representative SEM images of carbon fibers after the oxidation of PMMA-*b*-PAN fibers at 280 °C and carbonization at 800 °C. The polymer fibers were electrospun under R.H. of (a) 40%, (b) 50%, (c) 60%, (d) 70%, (e) 80%, and (f) 90%.

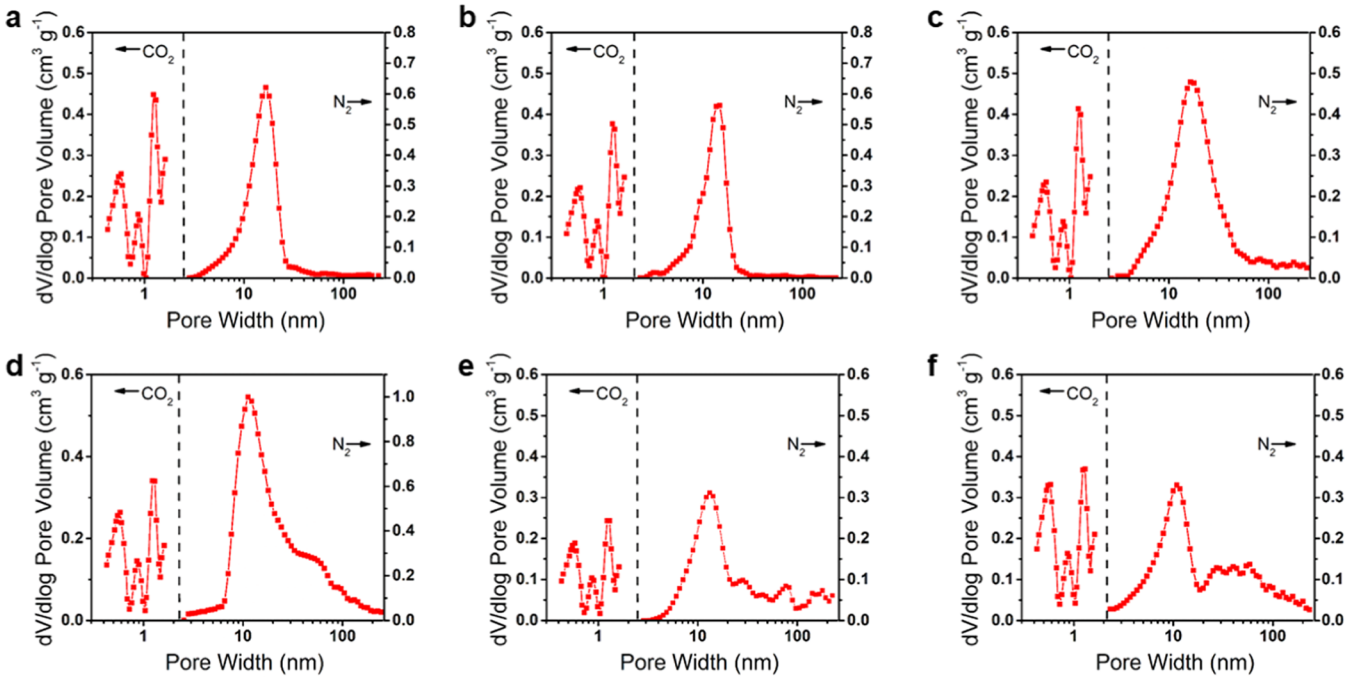

Figure 5. Pore width distributions of PCFs calculated using NLDFT based on the physisorption of N_2 for mesopores and CO_2 for micropores. The corresponding polymer fibers were electrospun under R.H. of (a) 40%, (b) 50%, (c) 60%, (d) 70%, (e) 80%, and (f) 90%.

templated by the PAN and PMMA domains that were kinetically trapped by electrospinning and PAN cross-linking (Figure 4a,b). The 60% PCFs started to show a slight pore size difference along the exterior of the fibers (Figure 4c). Reaching a critical point of the nonsolvent effect, the 70% PCFs showed nonuniform pore sizes, as well as a carbon sheath layer due to the PAN sheath developed during electrospinning and oxidation (Figure 4d). We expect these fibers to be flexible because of a continuous layer of carbon sheath.[60] The nonsolvent effect became more severe as the humidity level increased during electrospinning. The 80% carbon fibers exhibited ridge-like carbon structures derived from PAN, leaving behind grooves on the fiber skin surface (Figure 4e). Similarly, the 90% PCFs possessed nonuniform pore shapes in the cross section arising from more nonsolvent-induced phase separation than low-humidity fibers.[61,62]

The phase separation of block copolymer affects the physical properties of the fibers including pore size, surface area, and pore distribution. PMMA domains generate pores, but the coalescent PMMA domains increase the pore size, reduce the number of pores, and thus potentially decrease the overall surface area. The PMMA domains tend to reorganize toward the fiber interior during high-humidity electrospinning. The PAN sheath layer therefore encapsulates the pores inside the carbon fibers and makes them inaccessible. The potentially less pore connectivity, broader pore distribution, and more pore coalescence contributed to a decrease in surface area for high-humidity fibers (80−90% R.H.). A portion of the carbonized

https://doi.org/10.1021/acsapm.2c00534
ACS Appl. Polym. Mater. 2022, 4, 4980−4992

fibers develops disconnected pores due to the PMMA aggregation that evolved into macropores upon carbonization. The reorganization also induces the fibers to shift from a conventional cylindrical shape (40−60% humidity) to a nonuniform clumping shape with the formation of beads (80−90% humidity) (Figure S6). Overall, SEM suggests a decreasing surface area, pore volume, and pore uniformity as the humidity level increases (Figure S7).

Physisorption of PCFs. Physisorption revealed the pore size and surface areas of PCFs. N_2 isotherms of the PCFs showed type IV characteristics (Figure S8) and CO_2 isotherms showed type I characteristics (Figure S9), as defined by the International Union of Pure and Applied Chemistry (IUPAC).[63] Based on the quantity of gas adsorbed and the hysteresis, N_2 isotherms provided insights into mesopore sizes (2−50 nm), mesopore volumes, and surface areas, whereas CO_2 isotherms provided information about the micropores (<2 nm).

By applying nonlinear density functional theory (NLDFT) to both N_2 and CO_2 physisorption, the pore width distributions were obtained (Figure 5).[63] The 40% PCFs showed a clearly defined unimodal mesopore peak at ∼14 nm (Figure 5). The 50% PCFs displayed a similar unimodal peak centered at ∼15 nm with similar pore volumes. At 60% R.H., the PCF mesopore size was centered at ∼17 nm and the pore size dispersity increased, as evidenced by the increasing full width at half-maximum (FWHM). For the 70% PCFs, the FWHM further increased, and a shoulder appeared at >30 nm, but the mesopore size did not change drastically from the 60% PCFs. The unimodal mesopore peak nearly disappeared at 80−90% humidity, and the population of mesopores >20 nm notably increased. In addition, the overall pore volumes of 80 and 90% PCFs drastically decreased (Figures 5 and 7 and Table 2). The micropores in all PCFs were trimodal and centered about ∼0.58, 0.86, and 1.2 nm (Figure 5). We attribute the micropores to missing graphitic layers within PAN-derived carbon, which is present throughout all PCFs and PAN-derived carbon fibers.[45,64]

Table 2. Surface Area, Pore Volume, and Peak Mesopore Size Based on Nitrogen Physisorption Data for 40−90% PCFs

R.H. (%)	surface area ($m^2\ g^{-1}$)	mesopore volume ($cm^3\ g^{-1}$)	peak mesopore size (nm)
40	567	0.487	∼14
50	559	0.491	∼15
60	545	0.512	∼17
70	536	0.572	∼16
80	383	0.102	∼13
90	231	0.053	∼12

The PCF surface area and pore width distributions reflected similar trends to the microscopic observations of block copolymer morphologies from SEM. The pore volume for 40% PCFs was 0.487 $cm^3\ g^{-1}$. The pore volume increased with humidity up to 0.572 $cm^3\ g^{-1}$ (at 70% R.H.) and then drastically decreased with humidity down to 0.053 $cm^3\ g^{-1}$ (at 90% R.H.) (Table 2). The coalescence of the PMMA domains was observed in the SEM images (for both the polymer and oxidized fibers) and confirmed by physisorption. The coalescent PMMA domains generated merged mesopores and reduced the overall pore volume. Moreover, at 80 and 90% R.H., the nonsolvent-induced phase separation became a dominant effect that further reduced the pore uniformity and pore volume. Lastly, the PAN layer created a carbon sheath, which also likely decreased the accessible internal pore volume.

USAXS/SAXS Characterization of PCFs. USAXS/SAXS was used to investigate the morphological evolution of the electrospun mats. Merged USAXS/SAXS profiles for the spun fibers (Figure 6a) show a knee between q = 0.02 and 0.1 nm^{-1}, which is attributed to dimensions of the phase-separated domains between PAN and PMMA, in agreement with the SEM data in Figure 2. These USAXS/SAXS data also show a knee between q = 0.002 and 0.02 nm^{-1}, associated with the diameter of the spun fiber. Intensity oscillations present for the fiber diameter feature spun at 60, 70, and 80% relative humidities in the range of q = 0.008−0.02 nm^{-1} are associated with a form factor for rods of low polydispersity. At 40% R.H., DMF quickly evaporates during electrospinning, such that no phase separation occurs. As R.H. increases from 50 to 80%, the vapor-induced phase separation increases, leading to distinct knees in the scattering profiles. At 90% R.H., the scattering profiles again become featureless, suggesting a phase mixed morphology. Since PAN is slightly more hydrophilic than PMMA, PAN partitions toward the surfaces of high R.H. fibers, which may hinder further phase separation.

The USAXS and SAXS profiles for oxidized fibers were combined (Figure 6b). A feature between 0.06 and 0.3 nm^{-1} and a feature between q = 0.3 and 1 nm^{-1} are observed in the scattering profiles for the oxidized fibers, in addition to the fiber diameter feature between q = 0.002 and 0.02 nm^{-1}. Many concurrent processes, such as further phase development, PAN cross-linking, and PMMA degradation, occur during oxidation, making feature assignment challenging. The larger feature, between q = 0.06 and 0.3 nm^{-1}, likely arises due to PMMA and PAN phase separation, and the smaller feature, between q = 0.3 and 1 nm^{-1}, is likely due to the emergence of small pores. Nevertheless, neither feature size trends strongly with relative humidity.

USAXS/SAXS profiles for the pyrolyzed fibers are seen in Figure 6c. The fiber diameter feature is observed between q = 0.001 and 0.03 nm^{-1}, while the pore feature is observed from q = 0.03 to 5 nm^{-1}. At the lower humidity values of 40−50% R.H., pore features are observed at larger scattering vectors. At these humidity values, the scattering profile displays a broad peak shape, indicating that the pores are ordered relatively close together. At the high R.H. values of 70−90%, pore features are observed at lower scattering vectors. At these humidity values, the scattering profile displays a knee shape with no upturn, indicating that the pores are relatively dilute. At the intermediate R.H. of 60%, no strong scattering is observed, perhaps indicating that no single morphology is dominant.

USAXS/SAXS profiles were fit to the Unified Fit function to extract the radius of gyration of the features (Figure 7). Due to the irregular shape of the phase-separated domains and the pores, quantifying size with the shape-independent radius of gyration is reasonable. In characterizing the average dimensions of the pores (voids, postcarbonization), the radius of gyration, R_g, may be generally considered as the root-mean-square distance from the center of the void to the outer edges of the void. The radius of gyration of the phase-separated domains observed in the electrospun mats was found to be within 70 and 40 nm, with a minimum of 39.2 nm at 70% R.H. Over the range of relative humidity, the features observed in

https://doi.org/10.1021/acsapm.2c00534
ACS Appl. Polym. Mater. 2022, 4, 4980−4992

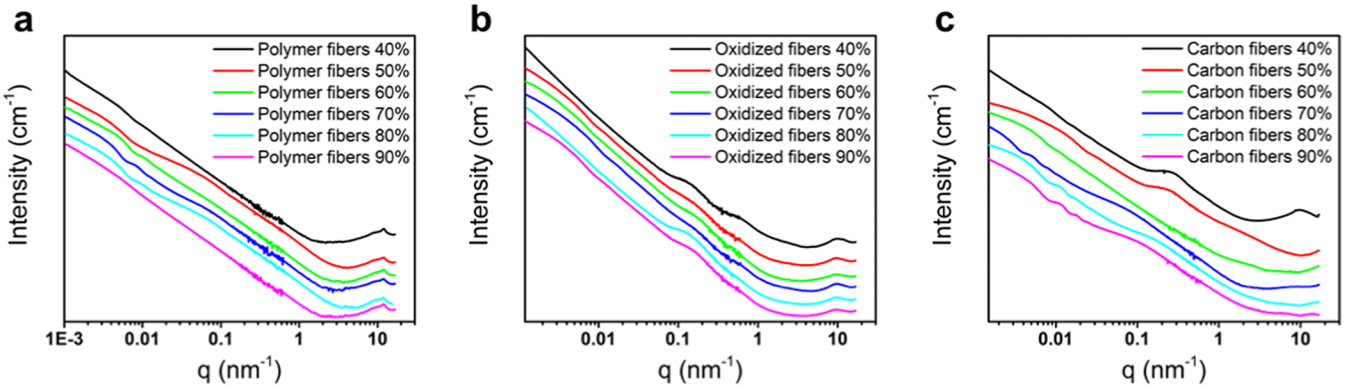

Figure 6. USAXS/SAXS profiles of (a) the as-spun block copolymer fiber mats under R.H. of 40−90% and the corresponding (b) oxidized fibers and (c) PCFs (carbonized).

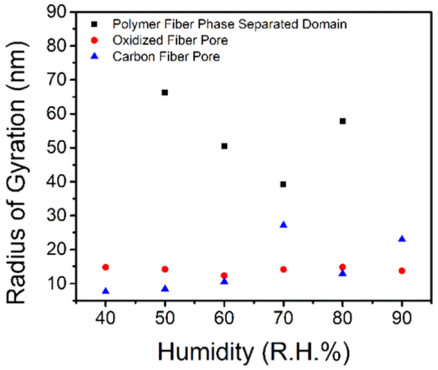

Figure 7. Radius of gyration (Unified Fit) of the fibers in the as-spun polymer, oxidized, and carbonized states as a function of R.H. (40−90%).

the oxidized fibers appear independent of relative humidity. The oxidized mats have a feature with a radius of gyration around 14 nm, attributed to the phase-separated domains, and another feature with a radius of gyration of about 4 nm, attributed to the pores (Figure 7).

USAXS/SAXS profiles from pyrolyzed samples were fit to the Unified Fit function (Table S1). Pore radii of gyration of 7.6 and 8.4 nm were found for the 40 and 50% R.H. samples, respectively. Assuming spherical pores, the pore radii can be calculated using the following equation[63]

$$R_g = \sqrt{\frac{3}{5}} R \tag{6}$$

The spherical radii for 40 and 50% then become 9.9 and 10.8 nm, respectively. These radii values agree with the porosimetry data, considering that the Guinier approximation overestimates the radius of gyration.[64] The Unified Fit function was modified with the Born−Green closure to the Ornstein−Zernicke equation to capture the structure found in the 40 and 50% R.H. samples. The correlation radius increases from 20.3 to 22.5 nm with increasing R.H. from 40 to 50%. Additionally, the packing factor decreases from 2.81 to 1.57 with increasing R.H. from 40 to 50%. These trends in the radius of correlation and packing factor indicate that the pores are less ordered at 50% R.H. Beyond 50% R.H., there is minimal influence of structure in the scattering patterns.

Increasing the relative humidity generally increases the radius of gyration of the pores (Figure 7), in agreement with the pore size distributions from nitrogen sorption. Similar to the BET and SEM results, the pore coalescence appears probably owing to the phase development of PMMA, which results in pore generation in the PCFs. The largest pores, with a radius of gyration of 27.2 nm, are observed with the samples spun at 70% R.H. This relative humidity may provide enough thermodynamic driving force to develop phases that are an optimal size and distribution for coalescence during pyrolysis. At higher relative humidity, fewer pores are present along the sheath region of the fibers (Figure S6), yet the PMMA domains coalesce creating larger pore sizes (Figure 5) due to

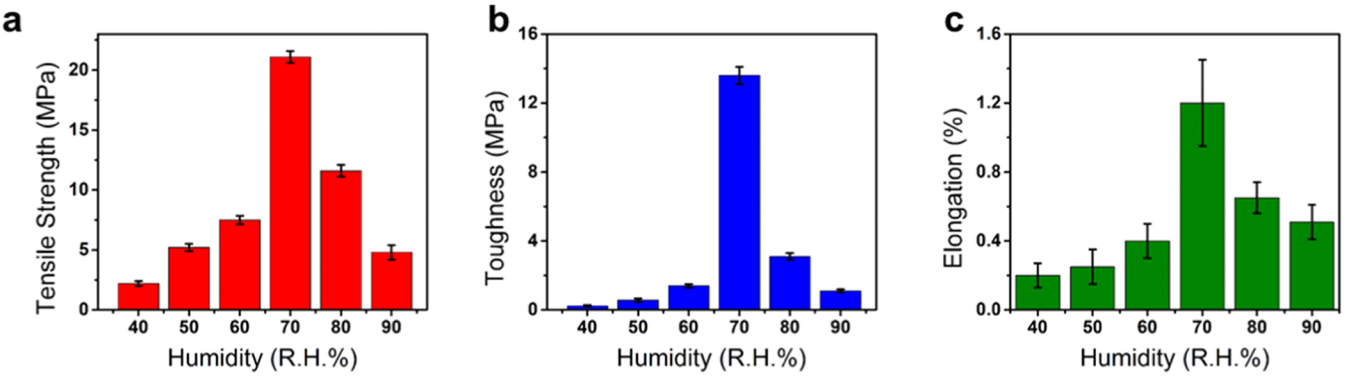

Figure 8. (a) Tensile strength, (b) toughness, and (c) elongation of PCF derived from polymer fibers electrospun under varying R.H. levels of 40−90%.

https://doi.org/10.1021/acsapm.2c00534
ACS Appl. Polym. Mater. 2022, 4, 4980−4992

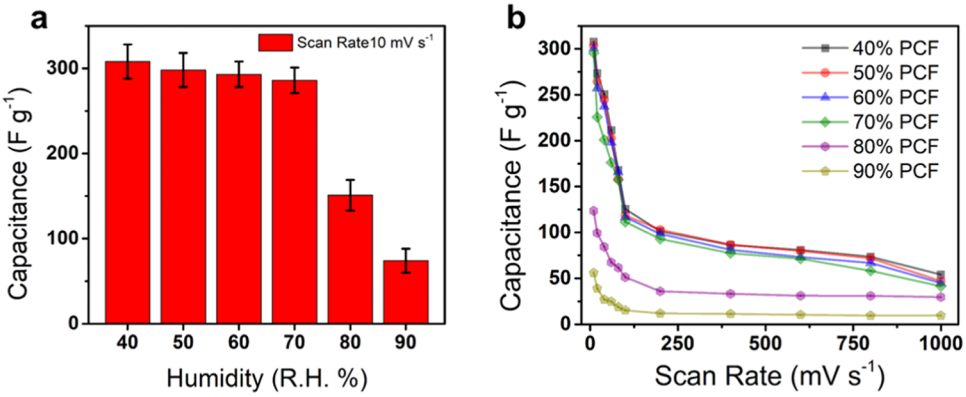

Figure 9. Electrochemical gravimetric capacitance of PCFs in 3 M KOH. (a) Gravimetric capacitance of PCFs *vs* R.H. at a scan rate of 10 mV s^{-1}. (b) Scan rate capacitance for PCFs in the range of 10−1000 mV s^{-1}. The percentage in the legend represents the R.H. during electrospinning of the fibers.

less well-developed phase separation. Notably, the pyrolyzed pore radius of gyration ends up between the values for the oxidized phase-separated domain size and the oxidized pore radius of gyration for the low R.H. values (Figure 2). This observation may indicate that the pores are growing as the domains are shrinking and developing into pores. At the higher relative humidity values of 70 and 90%, the pyrolyzed pores are larger than the oxidized phase-separated domains. The coalescence of several pores may allow growth to larger sizes than the phase-separated domains. At 50 and 60% R.H., a smaller feature is seen between 1 and 5 nm^{-1}. This feature could indicate the presence of smaller pores (<10 nm). Incidentally, the nitrogen porosimetry pore size distributions of the 50 and 60% R.H. pyrolyzed fibers also indicate an increase in the number of pores with widths smaller than 10 nm.

Mechanical Properties of PCFs. The varying porous structures within the PCFs contributed to different mechanical properties. As shown by tensile tests (Figures 10 and S10 and Table S2), the tensile strength was the lowest for 40% PCFs and increased steadily with humidity up to 70%. The tensile strength of 70% PCFs was ∼5-fold that of 40% PCFs and at least 2-fold that of the rest of the PCF mats (Figure 8a). The 80% PCFs exhibited the second highest tensile strength but still only half the strength of the 70% PCFs. As the humidity further increased to 90%, the tensile strength decreased. The toughness of PCFs showed a trend similar to tensile strength, where the 70% PCFs exhibited the highest (13 MPa) and 40% PCFs exhibited the lowest (<1 MPa) toughness (Figure 8b). Most PCFs showed <1% elongation, except the 70% PCFs, which exhibited 1.2% elongation (Figure 8c).

The development of a carbon sheath owing to polymer domain reorganization benefited the mechanical strength of certain PCFs. Typically, low-humidity PCFs (*i.e.*, 40 and 50%) lacked a continuous mechanically strong carbon structure present in conventional gel-spun PAN-derived carbon fibers.[65] Instead, they have a perforated carbon network around the pores. The network had "necking" regions, where stress could concentrate and reduce the overall axial resiliency during deformation.[66] The necking regions can be strengthened by tension during pyrolysis, similar to the tensioning conventional carbon fibers during the pyrolysis process.[67] As the relative humidity was increased from 40−50 to 60−80%, a continuous carbon sheath layer was developed in the PCFs. The long-range carbon sheath layer increased the mechanical strength of the fiber mats. Particularly, the 60 and 70% PCFs exhibited good flexibility despite the high porosity. The 80% PCFs possessed low porosity and good flexibility, but the bead-and-clump formation, which was caused by the nonsolvent precipitation, diminished the mechanical strength of the fiber mat (Table S2). Our results agreed with observations in a previous report,[68] where electrospun PMMA fibers from DMF solutions showed a similar critical relative humidity level at 80%. At ∼80% R.H., the nonsolvent effect reached a tipping point and it started to distort the fiber morphologies (Figure S11). Lastly, the 90% PCFs lacked flexibility, likely because the carbon sheath layer was disrupted by the bead-and-clump structures induced by the severe nonsolvent VIPS and polymer precipitation. In addition to the carbon sheath layer, USAX data indicated that the 70% PCFs had the largest average fiber diameter, which also contributed to the strongest mechanical strength (Figure S12). The larger diameter likely contributed to more graphitic stacking of the carbon atoms, and thus the fiber mats show higher tensile strength. In addition to the carbon sheath layer, USAX data indicated that the 70% PCFs had the largest average fiber diameter, which also contributed to the strongest mechanical strength (Figure S10). The larger diameter likely contributed to more graphitic stacking of the carbon atoms, and thus the fiber mats show higher tensile strength. Overall, the 70% PCFs showed the highest flexibility because of the continuous carbon sheath and large fiber diameter.

Electrochemical Performance of PCFs. Owing to the conductivity of graphitic carbon, PCFs have excellent potential for use as electrodes in energy storage. The gravimetric capacitances of all PCFs were examined in a 3 M KOH aqueous solution using a three-electrode cell with a Ag/AgCl reference electrode. At a 10 mV s^{-1} scan rate, the 40−70% PCFs displayed the highest capacitances of ∼300 F g^{-1} (Figure 9a). However, capacitance dropped by roughly half for the 80% PCFs (153 F g^{-1}) and by another half for the 90% PCFs (71 F g^{-1}). The scan rate capacitance of the PCFs followed tantamount trends across the range of 10−1000 mV s^{-1} (Figure 9b). Surface area correlates positively with the electric double-layer capacitance of porous materials. Because of the similar surface areas (difference within ±16 m^2 g^{-1} from the average), the capacitance of 40−70% PCFs was comparable (difference within ±12 F g^{-1} from the average) (Figure S13). Additionally, there was pseudo-capacitance contributed by the N and O heteroatomic doping, which resulted from PAN and oxidation.

https://doi.org/10.1021/acsapm.2c00534
ACS Appl. Polym. Mater. 2022, 4, 4980−4992

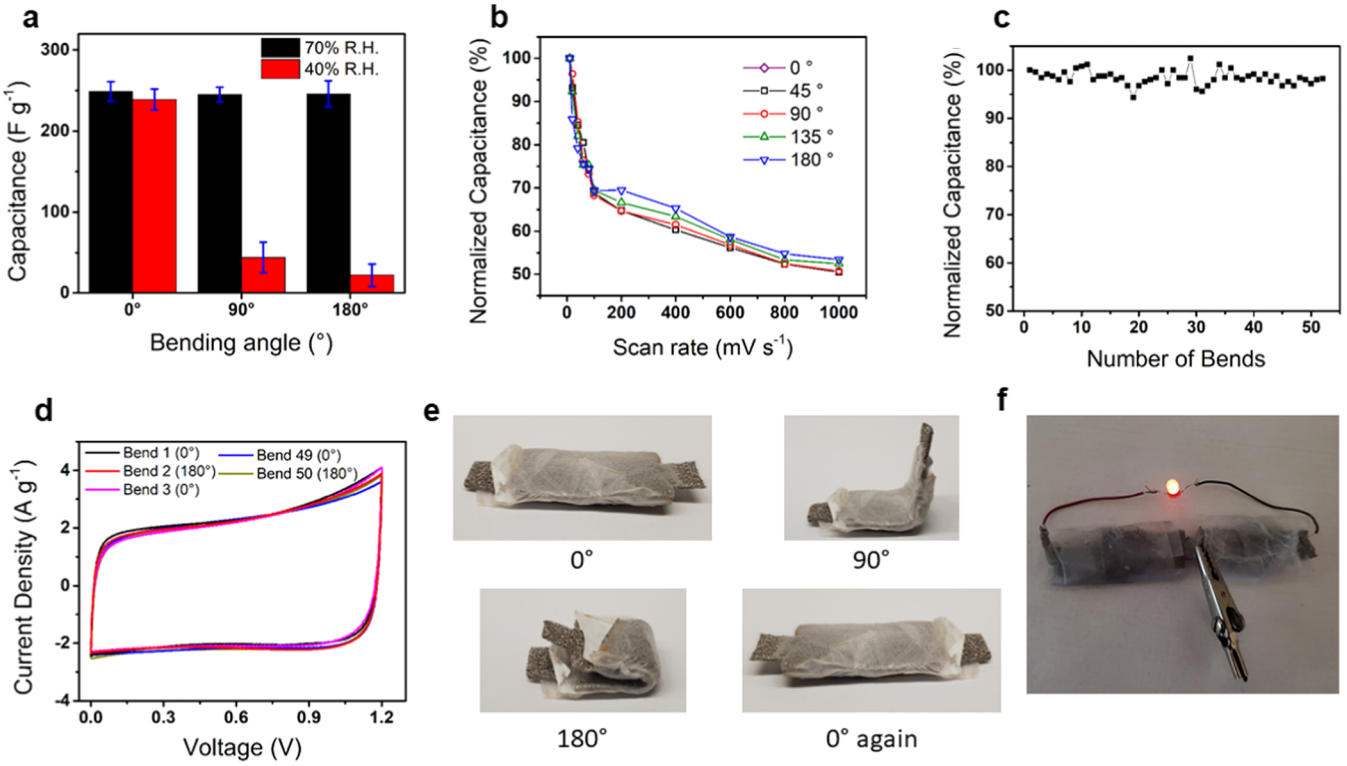

Figure 10. Electrochemical performance of PCFs within the gel-state electrolyte (PVA/KOH). (a) Gravimetric capacitance of 40 and 70% PCFs at 0, 90, and 180° at a 10 mV s^{-1} scan rate. (b) Rate capacitance of the 70% PCFs at bending angles of 0, 45, 90, 135, and 180° at scan rates of 10−1000 mV s^{-1}. (c) Normalized capacitance for the 70% PCFs upon repeated bending and (d) representative CV curves at 20 mV s^{-1} in the first three and last two bending cycles. The bending angles are shown in parentheses. (e) Photographs of a capacitor made of the 70% PCFs bent at angles of 0 to 90, 180°, and back to 0°. (f) A photograph of a lit LED bulb with two PCF capacitors in series.

Based on the physical, mechanical, and electrochemical performances of the PCFs, the electrodes were investigated for use in flexible supercapacitors. The 40 and 70% PCFs were evaluated within a polyelectrolyte cell of PVA/KOH wrapped by a parafilm. The electrodes were bent at various angles between 0 and 180°, and the capacitances were measured with cyclic voltammetry (Figure 10). At 0°, both 40 and 70% PCFs exhibited congruous specific capacitances of 239 ± 12 and 249 ± 13 F g^{-1}, respectively. At 90°, however, only the 70% PCFs retained the same performance, while the 40% PCFs dropped their capacitance by ∼82% (Figure 10a). At 180°, the 70% PCFs retained the structure and capacitance of 249 ± 20 F g^{-1}, while the 40% PCFs reduced further down to 22 ± 14 F g^{-1}. Ultimately, the 70% PCFs provided reliable gravimetric capacitances upon being bent at various angles, whereas the 40% PCFs lost the energy storage capabilities. The 70% PCFs were then subjected to bend angles of 0, 45, 90, 135, and 180° at scan rates of 10−1000 mV s^{-1} (Figure 10b). The 70% PCFs showed a 52 ± 4% retention capability regardless of the bending angle. One consideration for the flexible electrodes was the ability to survive repeated bending. The 70% PCFs were bent between 0 and 180° for 50 cycles, and the capacitances were measured at 20 mV s^{-1} (Figure 10c). At the 50th bend, the fibers showed an ∼99% capacitance retention (Figure 10c). Two in-series capacitors made of ∼3 mg of 70% PCFs provided a voltage of ∼2.2 V and were able to light a simple light-emitting diode (LED) (Figure 10e). Although rudimentary, the PCFs demonstrated the capability for developing advanced flexible electronics, where PCFs can serve as both structural support and energy storage media.

CONCLUSIONS

Block copolymer-derived PCFs hold significant promise in developing advanced structural energy materials. Electrospinning conditions of the polymer fibers provided a way to tune the mechanical and electrochemical properties of PCFs. In conjunction with block copolymer microphase separation, the use of a nonsolvent such as water vapor jointly controlled the porosity and mechanical properties *via* VIPS. In the low-humidity range (40−50% R.H.), water vapor showed little effect and PMMA-*b*-PAN fibers mainly underwent microphase separation, which developed into mesopores with narrow pore width distributions. In the mid-humidity range (60−70% R.H.), water vapor provided enough driving forces to initiate a VIPS effect, reorganizing the PAN and PMMA domains to form a core−sheath structure in the fibers. Lastly, in the high-humidity range (80−90% R.H.), the fibers experienced strong vapor-induced phase separation and even precipitation, forming large polymer clusters and thus nonuniform pores in the PCFs that severely weakened the mechanical strength. The electric double-layer capacitance favored the lower humidity owing to the higher surface areas. The juxtaposition of both flexibility and electric double-layer capacitance existed at 70% R.H., showing a window for PCFs to achieve both electrochemical and mechanical properties. Fabricated into flexible capacitors, the 70% PCFs demonstrated the capability of serving as structural energy storage materials. The morphological study herein provides a systematic understanding of nonsolvent effects on electrospun block copolymer fibers and the resulting PCFs. The flexible block copolymer-derived PCFs

https://doi.org/10.1021/acsapm.2c00534
ACS Appl. Polym. Mater. 2022, 4, 4980−4992

underscore the potential in flexible electronics, energy storage, and environmental science.

■ ASSOCIATED CONTENT

Supporting Information

The Supporting Information is available free of charge at https://pubs.acs.org/doi/10.1021/acsapm.2c00534.

Size exclusion chromatography, SEM images, stress−strain profiles, humidity related to pore volume, R_{g3} Unified Fit and elongation, surface area compared to gravimetric capacitance, USAXS/SAXS unified fit function output, and DMA results (PDF)

■ AUTHOR INFORMATION

Corresponding Author

Guoliang Liu − *Department of Chemistry, Virginia Tech, Blacksburg, Montgomery County, Virginia 24061, United States; Macromolecules Innovations Institute and Division of Nanoscience, Academy of Integrated Science, Virginia Tech, Blacksburg, Montgomery County, Virginia 24061, United States;* orcid.org/0000-0002-6778-0625; Email: gliu1@vt.edu

Authors

Joel M. Serrano − *Department of Chemistry, Virginia Tech, Blacksburg, Montgomery County, Virginia 24061, United States;* orcid.org/0000-0002-1508-5508

Glenn A. Spiering − *Department of Chemistry, Virginia Tech, Blacksburg, Montgomery County, Virginia 24061, United States; Macromolecules Innovations Institute, Virginia Tech, Blacksburg, Montgomery County, Virginia 24061, United States*

Zhen Xu − *Department of Chemistry, Virginia Tech, Blacksburg, Montgomery County, Virginia 24061, United States*

Zacary Croft − *Department of Chemistry, Virginia Tech, Blacksburg, Montgomery County, Virginia 24061, United States*

Dong Guo − *Department of Chemistry, Virginia Tech, Blacksburg, Montgomery County, Virginia 24061, United States;* orcid.org/0000-0002-3469-2602

Ke Cao − *Macromolecules Innovations Institute, Virginia Tech, Blacksburg, Montgomery County, Virginia 24061, United States;* orcid.org/0000-0001-7204-7455

Robert B. Moore − *Department of Chemistry, Virginia Tech, Blacksburg, Montgomery County, Virginia 24061, United States; Macromolecules Innovations Institute, Virginia Tech, Blacksburg, Montgomery County, Virginia 24061, United States;* orcid.org/0000-0001-9057-7695

Complete contact information is available at: https://pubs.acs.org/10.1021/acsapm.2c00534

Author Contributions

The manuscript was written through the contributions of all authors. All authors have given approval to the final version of the manuscript.

Notes

The authors declare no competing financial interest.

■ ACKNOWLEDGMENTS

The authors acknowledge the use of the nanoscale characterization and fabrication laboratory (NCFL) and chemistry facilities at Virginia Tech. This research used resources of the Advanced Photon Source, a U.S. Department of Energy (DOE) Office of Science User Facility operated for the DOE Office of Science by Argonne National Laboratory under Contract No. DE-AC02-06CH11357. This material was based on the work supported by the National Science Foundation under the award number DMR-1752611 through the CAREER award, DMR-2104856, and the American Chemical Society Petroleum Research Foundation through the Doctoral New Investigator (DNI) award. USAXS/SAXS data were collected at the 9-ID-C beamline at the Advanced Photon Source, Argonne National Laboratory.

■ REFERENCES

(1) Huang, S.; Liu, Y.; Zhao, Y.; Ren, Z.; Guo, C. F. Flexible electronics: Stretchable electrodes and their future. *Adv. Funct. Mater.* **2019**, *29*, No. 1805924.

(2) Wang, X.; Jiang, K.; Shen, G. Flexible fiber energy storage and integrated devices: recent progress and perspectives. *Mater. Today* **2015**, *18*, 265−272.

(3) Shi, Y.; Yu, G. Designing hierarchically nanostructured conductive polymer gels for electrochemical energy storage and conversion. *Chem. Mater.* **2016**, *28*, 2466−2477.

(4) Jo, K.; Lee, S.; Kim, S.-M.; In, J. B.; Lee, S.-M.; Kim, J.-H.; Lee, H.-J.; Kim, K.-S. Stacked bilayer graphene and redox-active interlayer for transparent and flexible high-performance supercapacitors. *Chem. Mater.* **2015**, *27*, 3621−3627.

(5) Nguyen, T. T.; Balamurugan, J.; Aravindan, V.; Kim, N. H.; Lee, J. H. Boosting the energy density of flexible solid-state supercapacitors via both ternary NiV_2Se_4 and $NiFe_2Se_4$ nanosheet arrays. *Chem. Mater.* **2019**, *31*, 4490−4504.

(6) Ham, S.; Kang, M.; Jang, S.; Jang, J.; Choi, S.; Kim, T.-W.; Wang, G. One-dimensional organic artificial multi-synapses enabling electronic textile neural network for wearable neuromorphic applications. *Sci. Adv.* **2020**, *6*, No. eaba1178.

(7) Fong, K. D.; Wang, T.; Smoukov, S. K. Multidimensional performance optimization of conducting polymer-based supercapacitor electrodes. *Sustainable Energy Fuels* **2017**, *1*, 1857−1874.

(8) Heo, J. S.; Eom, J.; Kim, Y. H.; Park, S. K. Recent progress of textile-based wearable electronics: A comprehensive review of materials, devices, and applications. *Small* **2018**, *14*, No. 1703034.

(9) Yadav, A.; De, B.; Singh, S. K.; Sinha, P.; Kar, K. K. Facile development strategy of a single carbon-fiber-based all-solid-state flexible lithium-ion battery for wearable electronics. *ACS Appl. Mater. Interfaces* **2019**, *11*, 7974−7980.

(10) Zhang, M.; He, L.; Shi, T.; Zha, R. Nanocasting and direct synthesis strategies for mesoporous carbons as supercapacitor electrodes. *Chem. Mater.* **2018**, *30*, 7391−7412.

(11) Wang, F.; Wu, X.; Yuan, X.; Liu, Z.; Zhang, Y.; Fu, L.; Zhu, Y.; Zhou, Q.; Wu, Y.; Huang, W. Latest advances in supercapacitors: from new electrode materials to novel device designs. *Chem. Soc. Rev.* **2017**, *46*, 6816−6854.

(12) Hamedi, M. M.; Ainla, A.; Guder, F.; Christodouleas, D. C.; Fernandez-Abedul, M. T.; Whitesides, G. M. Integrating electronics and microfluidics on paper. *Adv. Mater.* **2016**, *28*, 5054−5063.

(13) Zhang, Y.; Zhang, L.; Cui, K.; Ge, S.; Cheng, X.; Yan, M.; Yu, J.; Liu, H. Flexible electronics based on micro/nanostructured paper. *Adv. Mater.* **2018**, *30*, No. e1801588.

(14) Casado, N.; Hernandez, G.; Veloso, A.; Devaraj, S.; Mecerreyes, D.; Armand, M. PEDOT radical polymer with synergetic redox and electrical properties. *ACS Macro. Lett.* **2016**, *5*, 59−64.

(15) Davoglio, R. A.; Biaggio, S. R.; Bocchi, N.; Rocha-Filho, R. C. Flexible and high surface area composites of carbon fiber, polypyrrole, and poly(DMcT) for supercapacitor electrodes. *Electrochim. Acta* **2013**, *93*, 93−100.

(16) Zhou, C.; Zhang, Y.; Li, Y.; Liu, J. Construction of high-capacitance 3D CoO@polypyrrole nanowire array electrode for aqueous asymmetric supercapacitor. *Nano Lett.* **2013**, *13*, 2078−2085.

(17) Islam, M. M.; Aboutalebi, S. H.; Cardillo, D.; Liu, H. K.; Konstantinov, K.; Dou, S. X. Self-assembled multifunctional hybrids: Toward developing high-performance graphene-based architectures for energy storage devices. *ACS Cent. Sci.* **2015**, *1*, 206−216.
(18) Choi, H.; Yoon, H. Nanostructured electrode materials for electrochemical capacitor applications. *Nanomaterials* **2015**, *5*, 906−936.
(19) Ates, M.; Eren, N.; Osken, I.; Baslilar, S.; Ozturk, T. Poly(2,6-di(thiophene-2-yl)-3,5bis(4-(thiophene-2-yl)phenyl)dithieno [3,2-b;2′,3′-d]thiophene)/carbon nanotube composite for capacitor applications. *J. Appl. Polym. Sci.* **2014**, *131*, 40061.
(20) Li, B.; Cheng, J.; Wang, Z.; Li, Y.; Ni, W.; Wang, B. Highly-wrinkled reduced graphene oxide-conductive polymer fibers for flexible fiber-shaped and interdigital-designed supercapacitors. *J. Power Sources* **2018**, *376*, 117−124.
(21) Rui, K.; Wang, X.; Du, M.; Zhang, Y.; Wang, Q.; Ma, Z.; Zhang, Q.; Li, D.; Huang, X.; Sun, G.; Zhu, J.; Huang, W. Dual-function metal-organic framework-based wearable fibers for gas probing and energy storage. *ACS Appl. Mater. Interfaces* **2018**, *10*, 2837−2842.
(22) He, Z.; Li, M.; Li, Y.; Zhu, J.; Jiang, Y.; Meng, W.; Zhou, H.; Wang, L.; Dai, L. Flexible electrospun carbon nanofiber embedded with TiO2 as excellent negative electrode for vanadium redox flow battery. *Electrochim. Acta* **2018**, *281*, 601−610.
(23) Tai, M. H.; Gao, P.; Tan, B. Y.; Sun, D. D.; Leckie, J. O. Highly efficient and flexible electrospun carbon-silica nanofibrous membrane for ultrafast gravity-driven oil-water separation. *ACS Appl. Mater. Interfaces* **2014**, *6*, 9393−401.
(24) Gopalsamy, K.; Xu, Z.; Zheng, B.; Huang, T.; Kou, L.; Zhao, X.; Gao, C. Bismuth oxide nanotubes-graphene fiber-based flexible supercapacitors. *Nanoscale* **2014**, *6*, 8595−8600.
(25) Liu, X.; Naylor Marlow, M.; Cooper, S. J.; Song, B.; Chen, X.; Brandon, N. P.; Wu, B. Flexible all-fiber electrospun supercapacitor. *J. Power Sources* **2018**, *384*, 264−269.
(26) Di Blasi, A.; Busaccaa, C.; Di Blasia, O.; Briguglioa, N.; Squadritoa, G.; Antonuccia, V. Synthesis of flexible electrodes based on electrospun carbon nanofibers with Mn_3O_4 nanoparticles for vanadium redox flow battery application. *Appl. Energy* **2017**, *190*, 165−171.
(27) Yu, D.; Zhai, S.; Jiang, W.; Goh, K.; Wei, L.; Chen, X.; Jiang, R.; Chen, Y. Transforming pristine carbon fiber tows into high performance solid-state fiber supercapacitors. *Adv. Mater.* **2015**, *27*, 4895−4901.
(28) Zhang, Y.; Zhang, L.; Yin, X.; Liu, Y.; He, Z.; Zhang, J. Effects of porosity on in-plane and interlaminar shear strengths of two-dimensional carbon fiber reinforced silicon carbide composites. *Mater. Des.* **2016**, *98*, 120−127.
(29) Sun, J.; Zeng, L.; Jiang, H. R.; Chao, C. Y. H.; Zhao, T. S. Formation of electrodes by self-assembling porous carbon fibers into bundles for vanadium redox flow batteries. *J. Power Sources* **2018**, *405*, 106−113.
(30) Miao, Y.-E.; Huang, Y.; Zhang, L.; Fan, W.; Lai, F.; Liu, T. Electrospun porous carbon nanofiber@MoS_2 core/sheath fiber membranes as highly flexible and binder-free anodes for lithium-ion batteries. *Nanoscale* **2015**, *7*, 11093−11101.
(31) Ran, F.; Wu, Y.; Jiang, M.; Tan, Y.; Liu, Y.; Kong, L.; Kang, L.; Chen, S. Nanocomposites based on hierarchical porous carbon fiber@ vanadium nitride nanoparticles as supercapacitor electrodes. *Dalton Trans.* **2018**, *47*, 4128−4138.
(32) Serrano, J. M.; Liu, T.; Khan, A. U.; Botset, B.; Stovall, B. J.; Xu, Z.; Guo, D.; Cao, K.; Hao, X.; Cheng, S.; Liu, G. Composition design of block copolymers for porous carbon fibers. *Chem. Mater.* **2019**, *31*, 8898−8907.
(33) Stamopoulos, A. G.; Tserpes, K. I.; Prucha, P.; Vavrik, D. Evaluation of porosity effects on the mechanical properties of carbon fiber-reinforced plastic unidirectional laminates by X-ray computed tomography and mechanical testing. *J. Compos. Mater.* **2016**, *50*, 2087−2098.
(34) Rice, R. W. Limitations of pore-stress concentrations on the mechanical properties of porous materials. *J. Mater. Sci.* **1997**, *32*, 4731−4736.
(35) Tian, L.; Ji, D.; Zhang, S.; He, X.; Ramakrishna, S.; Zhang, Q. A humidity-induced nontemplating route toward hierarchical porous carbon fiber hybrid for efficient bifunctional oxygen catalysis. *Small* **2020**, *16*, No. e2001743.
(36) Liu, T.; Zhou, Z.; Guo, Y.; Guo, D.; Liu, G. Block copolymer derived uniform mesopores enable ultrafast electron and ion transport at high mass loadings. *Nat. Commun.* **2019**, *10*, No. 675.
(37) Serrano, J. M.; Khan, A. U.; Liu, T.; Xu, Z.; Esker, A. R.; Liu, G. Capacitive organic dye removal by block copolymer based porous carbon fibers. *Adv. Mater. Interfaces* **2020**, *7*, No. 2000507.
(38) Wan, C. T.; Jacquemond, R. R.; Chiang, Y. M.; Nijmeijer, K.; Brushett, F. R.; Forner-Cuenca, A. Non-solvent induced phase separation enables designer redox flow battery electrodes. *Adv. Mater.* **2021**, *33*, No. e2006716.
(39) Islam, M. S.; Ang, B. C.; Andriyana, A.; Afifi, A. M. A review on fabrication of nanofibers via electrospinning and their applications. *SN Appl. Sci.* **2019**, *1*, No. 1248.
(40) Yi, H.; Li, D.; Lv, Z.; Li, R.; Ling, M.; Zhang, H.; Zheng, Q.; Li, X. Constructing high-performance 3D porous self-standing electrodes with various morphologies and shapes by a flexible phase separation-derived method. *J. Mater. Chem. A* **2019**, *7*, 22550−22558.
(41) Zhao, Q.; Feng, R. X.; Yousef, L.; Zhuang, F.; Xiao-Jie, L.; Wei, J.; Liang, W.; Chu, Y. Preparation of high strength poly-(vinylidenefluoride) porous membraneswith cellular structure via vapor-induced phase separation. *J. Membr. Sci.* **2018**, *549*, 151−164.
(42) Jiang, Y.; Fang, D.; Song, G.; Nie, J.; Chen, B.; Ma, G. Fabrication of core−shell nanofibers by single capillary electrospinning combined with vapor induced phase separation. *New J. Chem.* **2013**, *37*, 2917−2924.
(43) Ma, W.; Li, M.; Zhou, X.; Li, J.; Dong, Y.; Zhu, M. Three-dimensional porous carbon nanotubes/reduced graphene oxide fiber from rapid phase separation for a high-rate all-solid-state supercapacitor. *ACS Appl. Mater. Interfaces* **2019**, *11*, 9283−9290.
(44) Zhou, Z.; Liu, T.; Khan, A. U.; Liu, G. Block copolymer−based porous carbon fibers. *Sci. Adv.* **2019**, *5*, No. eaau6852.
(45) Zhou, Z.; Liu, T.; Khan, A. U.; Liu, G. Controlling the physical and electrochemical properties of block copolymer-based porous carbon fibers by pyrolysis temperature. *Mol. Syst. Des. Eng.* **2020**, *5*, 153−165.
(46) Ilavsky, J.; Zhang, F.; Andrews, R. N.; Kuzmenko, I.; Jemian, P. R.; Levine, L. E.; Allen, A. J. Development of combined microstructure and structure characterization facility for in situ and operando studies at the Advanced Photon Source. *J. Appl. Crystallogr.* **2018**, *51*, 867−882.
(47) Ilavsky, J.; Jemian, P. R.; Allen, A. J.; Zhang, F.; Levine, L. E.; Long, G. G. Ultra-small-angle X-ray scattering at the Advanced Photon Source. *J. Appl. Crystallogr.* **2009**, *42*, 469−479.
(48) Ilavsky, J. Nika: software for two-dimensional data reduction. *J. Appl. Crystallogr.* **2012**, *45*, 324−328.
(49) Beaucage, G. Approximations leading to a unified exponential/power-law approach to small-angle scattering. *J. Appl. Crystallogr.* **1995**, *28*, 717−728.
(50) Beaucage, G.; Ulibarri, T. A.; Black, E.; Schaefer, D. Multiple Size Scale Structures in Silica-Siloxane Composites Studied by Small-Angle Scattering. In *ACS Symposium Series*; ACS: Washington, DC, 1995.
(51) Xie, R.; Luo, F.; Zhang, L.; Guo, S. F.; Liu, Z.; Ju, X. J.; Wang, W.; Chu, L. Y. A novel thermoresponsive catalytic membrane with multiscale pores prepared via vapor-induced phase separation. *Small* **2018**, *14*, No. e1703650.
(52) Pervin, R.; Ghosh, P.; Basavaraj, M. G. Tailoring pore distribution in polymer films via evaporation induced phase separation. *RSC Adv.* **2019**, *9*, 15593−15605.
(53) Wu, X.-F.; Salkovskiy, Y.; Dzenis, Y. A. Modeling of solvent evaporation from polymer jets in electrospinning. *Appl. Phys. Lett.* **2011**, *98*, No. 223108.

https://doi.org/10.1021/acsapm.2c00534
ACS Appl. Polym. Mater. 2022, 4, 4980−4992

(54) Liu, Y. C.; Lu, D. N. Surface energy and wettability of plasma-treated polyacrylonitrile fibers. *Plasma Chem. Plasma Process.* **2006**, *26*, 119−126.
(55) Owens, D. K.; Wendt, R. C. Estimation of the surface free energy of polymers. *J. Appl. Polym. Sci.* **1969**, *13*, 1741−1747.
(56) Fridrikh, S. V.; Yu, J. H.; Brenner, M. P.; Rutledge, G. C. Controlling the fiber diameter during electrospinning. *Phys. Rev. Lett.* **2003**, *90*, No. 144502.
(57) Bashir, Z. A critical review of the stabilisation of polyacrylonitrile. *Carbon* **1991**, *29*, 1081−1090.
(58) Li, X.-P.; Suo, X.-D.; Liu, Y.-D.; Li, Y.-H. Effect of gelation time on the microstructures, mechanical properties and cyclization reactions of dry-jet gel-spun polyacrylonitrile fibers. *New Carbon Mater.* **2019**, *34*, 9−18.
(59) Nayani, K.; Katepalli, H.; Sharma, C. S.; Sharma, A.; Patil, S.; Venkataraghavan, R. Electrospinning combined with nonsolvent-induced phase separation to fabricate highly porous and hollow submicrometer polymer fibers. *Ind. Eng. Chem. Res.* **2012**, *51*, 1761−1766.
(60) Natarajan, L.; New, J.; Dasari, A.; Yu, S.; Manan, M. A. Surface morphology of electrospun PLA fibers: mechanisms of pore formation. *RSC Adv.* **2014**, *4*, 44082−44088.
(61) Thommes, M.; Kaneko, K.; Neimark, A. V.; Olivier, J. P.; Rodriguez-Reinoso, F.; Rouquerol, J.; Sing, K. S. Physisorption of gases, with special reference to the evaluation of surface area and pore size distribution (IUPAC Technical Report). *Pure Appl. Chem.* **2015**, *87*, 1051−1069.
(62) Frank, E.; Hermanutz, F.; Buchmeiser, M. R. Carbon fibers: Precursors, manufacturing, and properties. *Macromol. Mater. Eng.* **2012**, *297*, 493−501.
(63) Roe, R.-J. *Methods of X-ray and Neutron Scattering in Polymer Science*; Oxford University Press on Demand, 2000.
(64) Kucheyev, S. O.; Toth, M.; Baumann, T. F.; Hamza, A. V.; Ilavsky, J.; Knowles, W. R.; Saw, C. K.; Thiel, B. L.; Tileli, V.; van Buuren, T.; et al. Structure of low-density nanoporous dielectrics revealed by low-vacuum electron microscopy and small-angle x-ray scattering. *Langmuir* **2007**, *23*, 1357−1362.
(65) De Vrieze, S.; van Camp, T.; Nelvig, A.; Hagström, B.; Westbroek, P.; De Clerck, K. The effect of temperature and humidity on electrospinning. *J. Mater. Sci.* **2009**, *44*, 1357−1362.
(66) Ni, X.; Cheng, W.; Huan, S.; Wang, D.; Han, G. Electrospun cellulose nanocrystals/poly(methyl methacrylate) composite nanofibers: Morphology, thermal and mechanical properties. *Carbohydr. Polym.* **2019**, *206*, 29−37.
(67) Ramachandran, J.; Lu, M.; Arias-Monje, P. J.; Kirmani, M. H.; Shirolkar, N.; Kumar, S. Towards designing strong porous carbon fibers through gel spinning of polymer blends. *Carbon* **2021**, *173*, 724−735.
(68) Medeiros, E. S.; Mattoso, L. H. C.; Offeman, R. D.; Wood, D. F.; Orts, W. J. Effect of relative humidity on the morphology of electrospun polymer fibers. *Can. J. Chem.* **2008**, *86*, 590−599.

https://doi.org/10.1021/acsapm.2c00534
ACS Appl. Polym. Mater. 2022, 4, 4980−4992